2009

Research on the Transport and Deposition of Nanoparticles in a Rotating Curved Pipe

Jianzhong Lin
Zhejiang University

Peifeng Lin
Zhejiang University

Huajun Chen
University of Nevada, Las Vegas

AIP | Physics of Fluids

Research on the transport and deposition of nanoparticles in a rotating curved pipe

Jianzhong Lin, Peifeng Lin, and Huajun Chen

Citation: Phys. Fluids **21**, 122001 (2009); doi: 10.1063/1.3264110
View online: http://dx.doi.org/10.1063/1.3264110
View Table of Contents: http://pof.aip.org/resource/1/PHFLE6/v21/i12
Published by the AIP Publishing LLC.

Research on the transport and deposition of nanoparticles in a rotating curved pipe

Jianzhong Lin,[1] Peifeng Lin,[1] and Huajun Chen[2]
[1]*State Key Laboratory of Fluid Power Transmission and Control, Zhejiang University, Hangzhou 310027, China and China Jiliang University, Hangzhou 310018, China*
[2]*Department of Mechanical Engineering, University of Nevada, Las Vegas, Nevada 89154, USA*

(Received 22 January 2009; accepted 22 July 2009; published online 14 December 2009)

A finite-volume code and the SIMPLE scheme are used to study the transport and deposition of nanoparticles in a rotating curved pipe for different angular velocities, Dean numbers, and Schmidt numbers. The results show that when the Schmidt number is small, the nanoparticle distributions are mostly determined by the axial velocity. When the Schmidt number is many orders of magnitude larger than 1, the secondary flow will dominate the nanoparticle distribution. When the pipe corotates, the distribution of nanoparticle mass fraction is similar to that for the stationary case. There is a "hot spot" deposition region near the outside edge of bend. When the pipe counter-rotates, the Coriolis force pushes the region with high value of nanoparticle mass fraction toward inside edge of the bend. The hot spot deposition region appears inside the edge. The particle deposition over the whole edge of the bend becomes uniform as the Dean number increases. The corotation of pipe makes the particle deposition efficiency a reduction, while high counter-rotation of pipe only slightly affects the deposition efficiency. When two kinds of secondary flows are coexisting, the relative deposition efficiency is larger than that for the stationary case. © *2009 American Institute of Physics*. [doi:10.1063/1.3264110]

I. INTRODUCTION

Our surroundings are filled with thousands of kinds of nanoparticles. A mechanism of the motion of these nanoparticles is of interest and has been investigated for decades. Nanoparticles suspended in pipes have lots of applications, such as enhanced heat transfer with nanoparticles in microheat exchangers, toxic particle transport in the human lung, contamination control of microelectronic manufacture, and control of surface fouling of microfluidic devices.[1–7]

When a pipe rotates about an axis normal to a plane including the center line of the pipe, the Coriolis force could also contribute to the generation of the secondary flow. Daskopoulos and Lenhoff[8] examined steady, fully developed Newtonian flow in circular rotating tubes of small curvature. They found that when rotation is in the same direction as the axial flow, the flow structure remains with two- or four-vortex secondary flow; when rotation opposes the flow, the direction of the secondary flow may be reversed at higher rotational strengths. Ma *et al.*[9] studied the fully developed laminar flow in rotating curved elliptical pipe. The simulation results showed that the flow for the case of large aspect ratio of the cross section is more likely to be unstable than that for smaller one. Ishigaki[10] studied on the forced convective heat transfer in loosely coiled rotating pipes theoretically and numerically. They studied the function of four characteristic parameters, i.e., the Dean number, the body force ratio F, the Rossby number, and the Prandtl number, and found that the former three parameters controlled the flow while the last one governed the heat transformation.

When the particle diameter is in the order of nanometer, the Brownian diffusion beside the inertial force is the dominant factor of the particle deposition.[11] Malet *et al.*[12] presented an experimental and numerical study of nanosize ^{218}Po deposition in laminar and turbulent tube flows. They observed an unexpected surface effect on nanoparticle deposition, even for a hydraulically smooth surface. An influence of surface texture on the deposition rate was observed too, which could be explained by a diffusion process, although all tube surfaces were hydraulically smooth. Zhang and Kleinstreuer[13] simulated and analyzed airflow structures and nanoparticle deposition in a human upper airway model for cyclic and steady flow conditions, using a commercial finite-volume software with user-supplied programs as a solver. Their results showed transient effects in the oral airways appear most prominently; total deposition fractions of nanoparticles for cyclic inspiratory flow are not significantly different from those for steady flow; more nanoparticles deposit around the carinal ridges than the straight tubular segments. Lin and Lin[14] simulated numerically the transport and deposition of nanoparticles in a bend pipe for different Reynolds numbers and Dean numbers, and found that the maximum and minimum of the deposition enhancement factor (DEF) occur near outside and inside edges of the bend, respectively.

It is obvious that the nanoparticulate flow in a curved pipe is much different from that in straight pipe. However, the previous investigations are generally focused on the nanoparticle deposit in straight pipe or stationary curved pipe. The nanoparticulate flow in a rotating curved pipe has not been examined in detail. When a curved pipe rotates about an axis normal to the pipe center line, the nanoparticle transfer and deposition will become more complicated. Therefore, this study is aimed to study the nanoparticle transport and deposition in a rotating curved pipe for different angular velocities, Dean numbers, and Schmidt numbers.

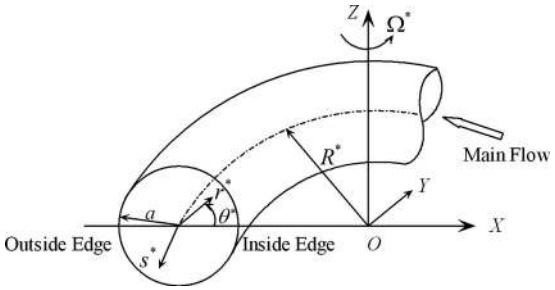

FIG. 1. Rotating curved pipe and coordinate system.

II. EQUATIONS AND PARAMETERS

The geometrical configuration of the physical model for a rotating curved pipe and its coordinate system are shown in Fig. 1. The pipe center line s^* is located in the X-Y plane, and the pipe rotates about the axis OZ with a constant angular velocity Ω^* (which is defined positive when anticlockwise rotating and negative when clockwise rotating). The coordinates r^* and θ^* are the polar coordinates defined on a given cross section of the pipe. The velocity components in the directions of (r^*, θ^*, s^*) are (u^*, v^*, w^*), respectively. The other geometrical parameters of the pipe are as follows: The radius of the pipe is a and the curvature radius of the bend is R^* (the bend curvature $\kappa^* = 1/R^*$). So the relations between the global rectangular Cartesian coordinates and the local toroidal coordinate system are

$$X = (R^* - r^* \cos\theta^*)\cos\frac{s^*}{R^*}, \quad Y = (R^* - r^* \cos\theta^*)\sin\frac{s^*}{R^*}, \quad Z = r^* \sin\theta^*. \tag{1}$$

Furthermore, the orthonormal basis $(\boldsymbol{e}_{r^*}, \boldsymbol{e}_{\theta^*}, \boldsymbol{e}_{s^*})$ is defined, relative to the global rectangular Cartesian basis $(\boldsymbol{i}, \boldsymbol{j}, \boldsymbol{k})$ as

$$\begin{aligned} \boldsymbol{e}_{r^*} &= -\boldsymbol{i}\cos\theta^*\cos\frac{s^*}{R^*} - \boldsymbol{j}\cos\theta^*\sin\frac{s^*}{R^*} + \boldsymbol{k}\sin\theta^*, \\ \boldsymbol{e}_{\theta^*} &= \boldsymbol{i}\sin\theta^*\cos\frac{s^*}{R^*} + \boldsymbol{j}\sin\theta^*\sin\frac{s^*}{R^*} + \boldsymbol{k}\cos\theta^*, \\ \boldsymbol{e}_{s^*} &= -\boldsymbol{i}\sin\frac{s^*}{R^*} + \boldsymbol{j}\cos\frac{s^*}{R^*}. \end{aligned} \tag{2}$$

In the system of rotating curved pipe, we can obtain the convective acceleration $\mathbf{a}_e^*$ and the Coriolis acceleration $\mathbf{a}_c^*$,

$$\begin{aligned} \mathbf{a}_e^* &= \frac{d\mathbf{V}_0^*}{dt^*} + \frac{d\boldsymbol{\Omega}^*}{dt^*} \times \mathbf{r}^* + \boldsymbol{\Omega}^* \times (\boldsymbol{\Omega}^* \times \mathbf{r}^*) \\ &= \boldsymbol{\Omega}^* \times (\boldsymbol{\Omega}^* \times \mathbf{r}^*) \\ &= \Omega^{*2}(R^* - r^* \cos\theta^*)\cos\theta^* \mathbf{e}_{r^*} \\ &\quad - \Omega^{*2}(R^* - r^* \cos\theta^*)\sin\theta^* \mathbf{e}_{\theta^*}, \end{aligned} \tag{3}$$

$$\mathbf{a}_c^* = 2\boldsymbol{\Omega}^* \times \mathbf{V}^* = 2\Omega^* \cos\theta^* w^* \mathbf{e}_{r^*} - 2\Omega^* \sin\theta^* w^* \mathbf{e}_{\theta^*} + 2\Omega^*(\sin\theta^* v^* - \cos\theta^* u^*)\mathbf{e}_{s^*}, \tag{4}$$

where $\boldsymbol{\Omega}^* = \Omega^* \mathbf{k}$, $\mathbf{V}_0^*$ is the translational velocity of the pipe, and $\mathbf{V}^*$ is the flow velocity relative to the rotating pipe.

By assuming that the flow is laminar, isothermal, and incompressible with monodisperse nanoparticle suspensions in the smooth rigid pipe, we can write the continuity and momentum equations of the fluid,

$$\nabla \cdot \mathbf{V}^* = 0, \tag{5}$$

$$\frac{D\mathbf{V}^*}{Dt^*} = -\frac{1}{\rho}\nabla p^* + \nu \Delta \mathbf{V}^* - \mathbf{a}_e^* - \mathbf{a}_c^*, \tag{6}$$

where ρ is the flow density, p^* is the pressure, and ν is the fluid kinematic viscosity.

The equation of the nanoparticle mass transfer is

$$\frac{DQ^*}{Dt^*} = \nabla \cdot [D_p(\nabla Q^*)] + S_Q, \tag{7}$$

where Q^* is the species mass fraction, S_Q is the source term and is neglected here in order to pay attention to the convection and diffusion of particles, and D_p is the diffusivity and defined as[15]

$$D_p = \frac{kTC_{\text{slip}}}{3\pi\mu d_p}, \tag{8}$$

where $k = 1.38 \times 10^{-23}$ J/K is the Boltzmann constant, T is the temperature, μ is the viscosity, d_p is the particle diameter, and C_{slip} is the Cunningham slip correction factor, which is calculated as

$$C_{\text{slip}} = 1 + \frac{\lambda}{d_p}\left[2.514 + 0.8\exp\left(-0.55\frac{d_p}{\lambda}\right)\right], \tag{9}$$

where λ is the mean free path of air.

Some nanoparticle diffusivities and Schmidt number with different nanoparticle diameters are given in Table I. The nondimensional variables are defined as

TABLE I. Some nanoparticle diffusivities and Schmidt number with different nanoparticle diameters.

d_p (nm)	0.5	5	20	50	80	100
D_p (m^2/s)	1.99×10^{-05}	2.02×10^{-07}	1.34×10^{-08}	2.29×10^{-09}	9.79×10^{-10}	6.64×10^{-10}
Sc	0.73	$7.24\times10^{+01}$	$1.11\times10^{+03}$	$6.37\times10^{+03}$	$1.49\times10^{+04}$	$2.20\times10^{+04}$

$$(r,s,R) = \frac{(r^*,s^*,R^*)}{d_h}, \quad \theta = \theta^*, \quad \kappa = \kappa^* d_h,$$

$$(u,v,w) = \frac{(u^*,v^*,w^*)}{w_m}, \quad p = \frac{d_h p^*}{\mu w_m},$$

$$\frac{\partial p^*}{\partial s^*} = -G, \quad w_m = \frac{G d_h{}^2}{4\mu}, \quad \mathrm{Re} = \frac{w_m d_h \rho}{\mu},$$

$$\mathrm{Dn} = \mathrm{Re}\sqrt{\kappa}, \quad Q = \frac{Q^*}{Q_m{}^*}, \quad \mathrm{Sc} = \frac{\mu}{\rho D_p}, \tag{10}$$

$$Q_m{}^* = -\mathrm{Sc}\ d_h \frac{\partial Q^*}{\partial s^*}, \quad \Omega = \frac{\Omega^* d_h{}^2 \rho}{\mu}, \quad \mathrm{Ro} = \frac{w_m}{\Omega^* d_h},$$

$$F = \frac{1}{\kappa\ \mathrm{Ro}} = \frac{\Omega^* d_h}{\kappa w_m}.$$

The variables with superscript * are the original variables and those without superscript * are the nondimensional variables, d_h is the characteristic length of the pipe and here $d_h = a$. Re is the Reynolds number, Dn is the Dean number, Sc is the Schmidt number, and F number represents the ratio of the Coriolis force to the centrifugal force. $F>0$, $F<0$, and $F=0$ represent the corotation, counter-rotation, and stationary cases, respectively. A generalized pressure $P = p - [\Omega^2 \nu (R - r\cos\theta)^2 / 2 d_h w_m]$ is defined so the contribution of the $\mathbf{a}_e$ can be contained into the term of pressure gradient in Eq. (6). For the fully developed laminar flow and nanoparticle transfer, we have $\partial/\partial t = 0$, $\partial u/\partial s = \partial v/\partial s = \partial w/\partial s = 0$,

$$\frac{\partial p}{\partial s} = \frac{\partial p^*}{\partial s^*}\frac{d_h{}^2}{\mu w_m} = -G\frac{d_h{}^2}{\mu w_m} = -\left(\frac{4\mu w_m}{d_h{}^2}\right)\frac{d_h{}^2}{\mu w_m} = -4$$

(Ref. 16), and

$$\frac{\partial Q}{\partial s} = \frac{\partial (Q^*/Q_m{}^*)}{\partial (s^*/d_h)} = \frac{\partial Q^*}{\partial s^*}\frac{d_h}{Q_m{}^*} = \frac{\partial Q^*}{\partial s^*}\frac{d_h}{-\mathrm{Sc}\ d_h\, \partial Q^*/\partial s^*} = -\frac{1}{\mathrm{Sc}}.$$

The boundary condition of particle concentration is $Q^* = 0$ at $r = 1$ for a perfectly absorbing surface of the wall.[15]

Before giving the control equations in detail, we first focus on the assumption of fully developed flow. In the experiment of Olson and Snyder[17] for the pipes, they took $\kappa = 0.215$ or 0.125, and the results show that the upstream influence extends 6a into a bend (in another word, the entrance region is about $0° < \phi < 74°$ or $0° < \phi < 43°$). Ishigaki[18] simulated the developing laminar flows numerically in curved pipes and orthogonally rotating straight pipes neglecting the axial diffusion. The computed results with both parabolic and uniform entrance show that the significant changes occur in the range of $15° < \phi < 45°$ for curved pipes ($1 < Z < 3$ for rotating straight pipes) at $K_L = 526, 100, 500$ (equal to $\mathrm{Dn} = 372, 71, 354$; $\kappa = 0.034, 0.025$ in current paper). Ma *et al.*[19] studied the laminar developing flow in the entrance region of rotation curved pipes. The result shows that at the cross section of $\phi = 30°$, the secondary flow has already been of two-vortex structure for both case of $F=1$ and $F=-1$ ($\mathrm{Dn}=141$, $\kappa=0.1$ in current paper). The entrance effect is obvious in the region of about $0° < \phi < 60°$, and the flow structure changes from sink type to two-vortex type. So we can see that when fluid flows through a curved pipe with 180° and small κ (e.g., $\kappa \le 0.1$), the entrance region is less than 1/3 of the entire curved pipe and the assumption of fully developed flow is worthwhile and creditable.

Accordingly, the continuity, momentum, and mass transfer equations governing the fully developed laminar flow and nanoparticle transfer can be obtained in terms of nondimensional variables as

$$\frac{\partial u}{\partial r} + \frac{1}{r}\frac{\partial v}{\partial \theta} + \frac{\kappa v \sin\theta}{M} + \frac{2u}{r} - \frac{u}{rM} = 0, \tag{11}$$

$$\mathrm{Re}\left(u\frac{\partial u}{\partial r} + \frac{v}{r}\frac{\partial u}{\partial \theta} - \frac{v^2}{r} + \frac{w^2\cos\theta\kappa}{M} + 2F\kappa w\cos\theta\right) = -\frac{\partial P}{\partial r} + \frac{\partial^2 u}{\partial r^2} + \frac{1}{r^2}\frac{\partial^2 u}{\partial \theta^2} + \left(-\frac{1}{r^2M^2} + \frac{2}{r^2M} - \frac{2}{r^2}\right)u + \left(\frac{\kappa\sin\theta}{rM^2} - \frac{2\kappa\sin\theta}{rM}\right)v + \left(\frac{2}{r} - \frac{1}{rM}\right)\frac{\partial u}{\partial r} - \frac{2}{r^2}\frac{\partial v}{\partial \theta} + \frac{\kappa\sin\theta}{rM}\frac{\partial u}{\partial \theta}, \tag{12}$$

$$\mathrm{Re}\left(u\frac{\partial v}{\partial r} + \frac{v}{r}\frac{\partial v}{\partial \theta} + \frac{uv}{r} - \frac{w^2\kappa\sin\theta}{M} - 2F\kappa w\cos\theta\right) = -\frac{1}{r}\frac{\partial P}{\partial \theta} + \frac{\partial^2 v}{\partial r^2} + \frac{1}{r^2}\frac{\partial^2 v}{\partial \theta^2} + \frac{\kappa u\sin\theta}{rM^2} + \left(\frac{1}{r^2M^2} - \frac{2}{r^2M} - \frac{\kappa^2}{M^2}\right)v + \left(\frac{2}{r} - \frac{1}{rM}\right)\frac{\partial v}{\partial r} + \frac{2}{r^2}\frac{\partial u}{\partial \theta} + \frac{\kappa\sin\theta}{rM}\frac{\partial v}{\partial \theta}, \tag{13}$$

$$\mathrm{Re}\left(u\frac{\partial w}{\partial r} + \frac{v}{r}\frac{\partial w}{\partial \theta} - \frac{uw\kappa\cos\theta}{M} + \frac{w\kappa\sin\theta}{M} + F(-2\kappa u\cos\theta + 2\kappa v\sin\theta)\right) = \frac{4}{M} + \frac{\partial^2 w}{\partial r^2} + \frac{1}{r^2}\frac{\partial^2 w}{\partial \theta^2} - \frac{w\kappa^2}{M^2} + \left(\frac{2}{r} - \frac{1}{rM}\right)\frac{\partial w}{\partial r} + \frac{\kappa\sin\theta}{rM}\frac{\partial w}{\partial \theta}, \tag{14}$$

$$\mathrm{Re}\left[\mathrm{Sc}\left(u\frac{\partial Q}{\partial r} + \frac{v}{r}\frac{\partial Q}{\partial \theta}\right) - \frac{w}{M}\right] = \frac{1}{r}\frac{\partial Q}{\partial r} + \frac{\partial^2 Q}{\partial r^2} + \frac{1}{r^2}\frac{\partial^2 Q}{\partial \theta^2} - \frac{\kappa\cos\theta}{M}\frac{\partial Q}{\partial r} + \frac{\kappa\sin\theta}{rM}\frac{\partial Q}{\partial \theta}, \tag{15}$$

where $M = 1 - \kappa r\cos\theta$.

In the present study, some important parameters for the transport and deposition of nanoparticles should be given out first. The diffusive mass transport rate per unit area to the wall based on Fick's first law can be defined as[15]

$$J_{\text{wall}} = -\rho \cdot D_p \cdot \nabla Q|_{\text{wall}}. \tag{16}$$

The ith local wall mass flux of nanoparticles can be determined by[13]

$$\dot{m}_i = -\rho A_i \cdot D_p \cdot \left.\frac{\partial Q}{\partial n}\right|_i, \tag{17}$$

where A_i is the area of the ith wall cell. The whole wall flow rate of nanoparticle is

$$\dot{m}_{\text{w}} = \rho \cdot D_p \cdot \sum^{\text{wall}} \left(\left.\frac{\partial Q}{\partial n}\right|_i \cdot A_i \right). \tag{18}$$

The DEF which can quantify the local nanoparticles deposition is defined as

$$\text{DEF}_i = \frac{\dot{m}_i/A_i}{\dot{m}_w/\Sigma^{\text{wall}} A_i}. \tag{19}$$

Obviously, DEF_i represents the local deposition flux intensity. The relative deposition efficiency to the stationary case is

$$\eta_r = \frac{\eta_d}{\eta_d|_{F=0}} = \frac{\dot{m}_w}{\dot{m}_w|_{F=0}}, \tag{20}$$

where η_r is the rotation contribution to the nanoparticle deposition.

III. NUMERICAL METHOD OF SOLUTION

A well-established finite-volume method[20] is used to study the flow and nanoparticle transport and deposition in a rotating curved pipe with circular cross section. The power-law scheme is chosen to discretize the convection term and the SIMPLE scheme to deal with the problem of velocity-pressure coupling. The power-law scheme is a piecewise approximation to the exact solution of a one-dimensional convection-diffusion type of equation. The scheme is numerically robust and always leads to physically realistic solution. A staggered mesh system with five refined boundary layers and an alternating direction implicit method are used to solve the two-dimensional discretized equations. Variables, such as pressure, axial velocity component w, and particle concentrations Q, are located at the centroids of the control volumes while the velocity components u and v on the cross section are located at the boundaries. A convergence criterion is specified with all the normalized residual errors for mass, u, v, w, and Q to be less than 10^{-4}. The boundary conditions in solution domain can be given as $u=v=w=0$ at $r=1$. The profile of nanoparticle concentrations at the inlet is uniform.

To validate the accuracy of the computational code, the fully developing flow patterns are compared to the numerical results given by Ishigaki[21] ($F_I=-2.0,-1.1,0,1.0$ at $K_{LC}=100$, $\lambda_I=50$) as shown in Figs. 2(a) and 2(b). The figure shows that the present results are in good agreements with previous results. It should be mentioned that there are some differences in detail of the coordinates and nondimensional parameters between Ishigaki[21] and present paper. The differences in the parameters give rise to the different expressions of the parameters in control equations. The relations are as follows: $\text{Re}=CK_{LC}{}^2\sqrt{\lambda_I}/32$, $F=16F_I/(K_{LC}C)$, and $\kappa=1/(2\lambda_I)$, where $C=d\sqrt{\lambda_I}(-\partial p^*/\partial z)/(\rho w_{mI}{}^2)$ is a constant depending on F_I and K_{LC} but unknown before solving a specific case. In present work, we employ a characteristic axial velocity based on pressure gradient [see Eq. (10)], thus we can avoid sinking into the extra work of obtaining the specific C by applying another iterative code during the computation.

To validate the numerical code in simulating the nanoparticle transport, we computed the distribution of nanoparticle mass fraction in the case of $F=0$ and $\kappa=0$, and compared the results to the theoretical results, as shown in Figs. 2(c) and 2(d). For the ultrafine particulate flow in a static straight pipe, we have $u=v=0$. Therefore, Eqs. (14) and (15) become

$$\frac{1}{r}\frac{\partial w}{\partial r} + \frac{1}{r^2}\frac{\partial^2 w}{\partial \theta^2} + \frac{\partial^2 w}{\partial r^2} = -4, \tag{21}$$

$$\frac{1}{r}\frac{\partial Q}{\partial r} + \frac{\partial^2 Q}{\partial r^2} + \frac{1}{r^2}\frac{\partial^2 Q}{\partial \theta^2} = -w\ \text{Re}. \tag{22}$$

Equations (21) and (22) are Poisson equations and have the following theoretical solutions:

$$w = 1 - r^2, \tag{23}$$

$$Q = \left(\tfrac{1}{16}r^4 - \tfrac{1}{4}r^2 + \tfrac{3}{16}\right)\text{Re}. \tag{24}$$

Figure 2(c) shows the theoretical result of nanoparticle mass fraction for $\text{Re}=200$, where Q has a maximum value 75/2 at $r=0$. We can also see that the both results are in good agreements.

IV. RESULTS AND DISCUSSION

The characteristic of the nanoparticle transport and deposition in a rotating curved pipe is affected by the interaction of the imposed pressure-driven axial flow, the rotation, and the geometrical structure of the pipe. The simultaneous presence of centrifugal and Coriolis forces will make the flow structure more complicated. The centrifugal force, as a result of curvature, will always point to the outside edge of the bend and push the flow with high axial velocity toward outside. The Coriolis force, as shown in Eq. (4), has three components, i.e., $2\Omega^* w^*(\cos\theta^* \mathbf{e}_{r^*} - \sin\theta^* \mathbf{e}_{\theta^*}) + 2\Omega^*(\sin\theta^* v^* - \cos\theta^* u^*)\mathbf{e}_{s^*}$. The first two terms, caused by the axial velocity, can also be written as $2\Omega^* w^* \mathbf{e}_{x^*}$, where $\mathbf{e}_{x^*}$ means a base vector that points to the rotation axis OZ from a given point and is parallel to the X-Y plane, i.e., pointing to the inside edge of bend. The first two terms contribute to the generation of secondary flow on the cross section. The last term in the direction of $\mathbf{e}_{s^*}$, caused by the secondary flow on the cross

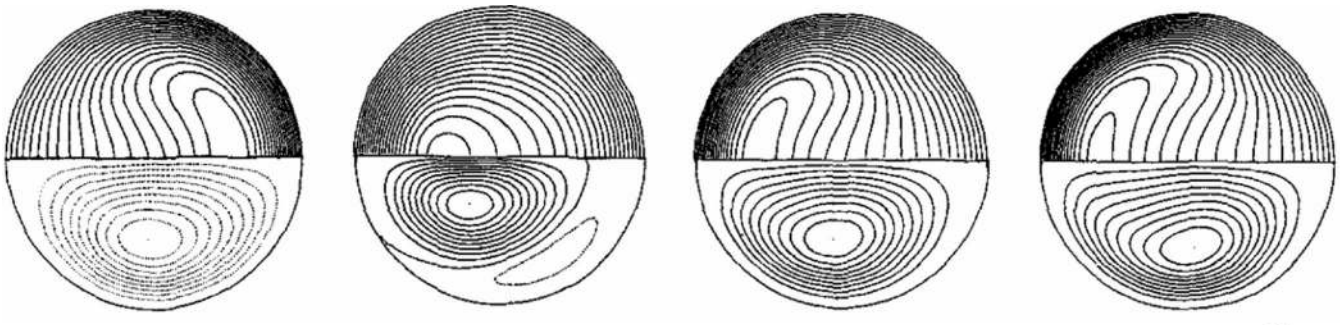

(a) Contours of axial velocity (upper-half) and secondary streamline (lower-half) given by Ishigaki[21]

$(F_I = -2.0,\ -1.1,\ 0,\ 1.0 \quad \text{at} \quad K_{LC} = 100, \lambda_I = 50)$

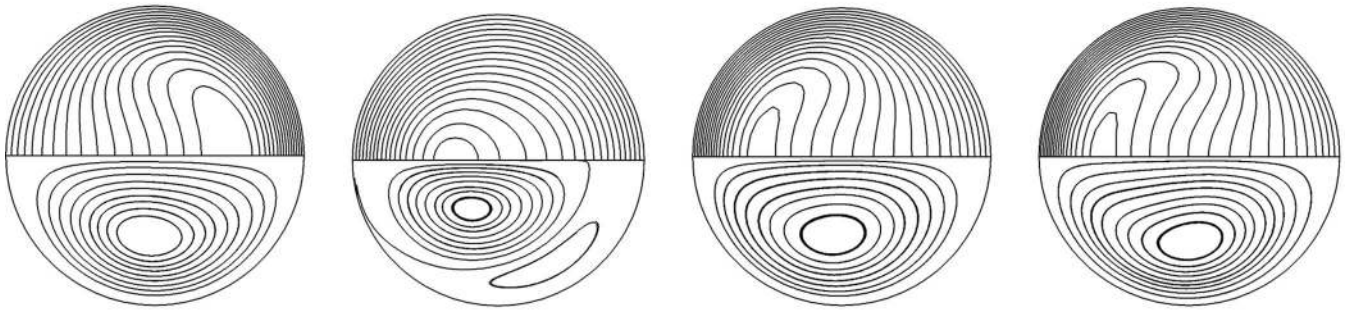

(b) Contours of axial velocity and secondary streamline given by present results.

$(F_I = -2.0,\ -1.1,\ 0,\ 1.0 \quad \text{at} \quad K_{LC} = 100, \lambda_I = 50)$

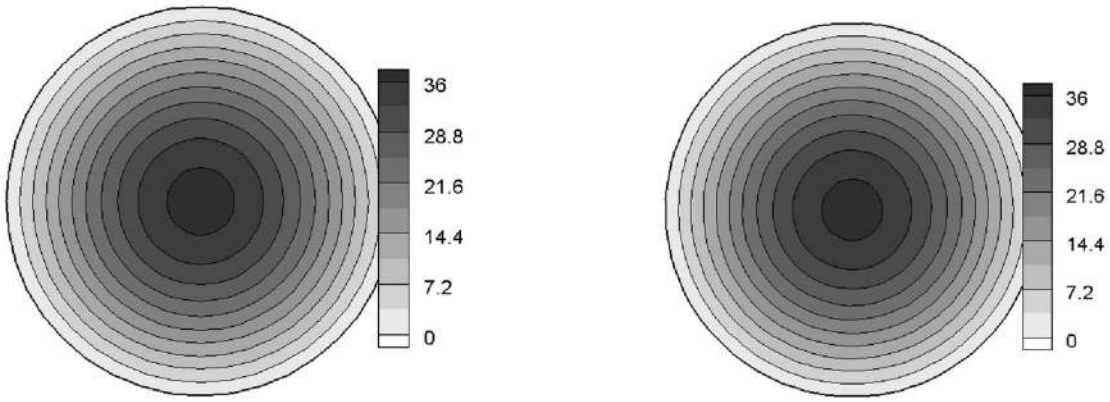

(c) theoretical result of nanoparticle mass fraction (d) present numerical result of nanoparticle mass fraction

$(F = 0, \kappa = 0, Re = 200)$

FIG. 2. Comparison of present numerical results with other results. (a) Contours of axial velocity (upper half) and secondary streamline (lower half) given by Ishigaki (Ref. 21) (F_I=−2.0,−1.1,0,1.0 at K_{LC}=100, λ_I=50). (b) Contours of axial velocity and secondary streamline given by present results (F_I=−2.0, −1.1,0,1.0 at K_{LC}=100, λ_I=50). (c) Theoretical result of nanoparticle mass fraction. (d) Present numerical result of nanoparticle mass fraction (F=0, κ =0, and Re=200).

section, will accelerate or decelerate the main flow and can be written as $-2\Omega^* u_{x^*}^* \mathbf{e}_{s^*}$, where $u_{x^*}^*$ is the velocity component in the base vector of $\mathbf{e}_{x^*}$.

A. Flow structures

The laminar flow in a curved duct has been well studied before,[8,10,21–23] thus we only give a brevity discussion here. Figure 3 shows the variation of the pressure contour, u-v components and w component (i.e., the axial velocity) on the cross section for different F numbers at Dn=63.25 and κ =0.1. The flow on the cross section is fully developed. For the stationary case (F=0), as shown in Fig. 3(a), the centrifugal force of the fluid points to the outside edge of the bend, which makes w large within the region near the outside edge. On the cross section, pressure has a positive value near the outside edge and a negative value near the inside edge of the bend. The slower moving fluid near the inside edge is driven toward the core region while the faster moving fluid near the

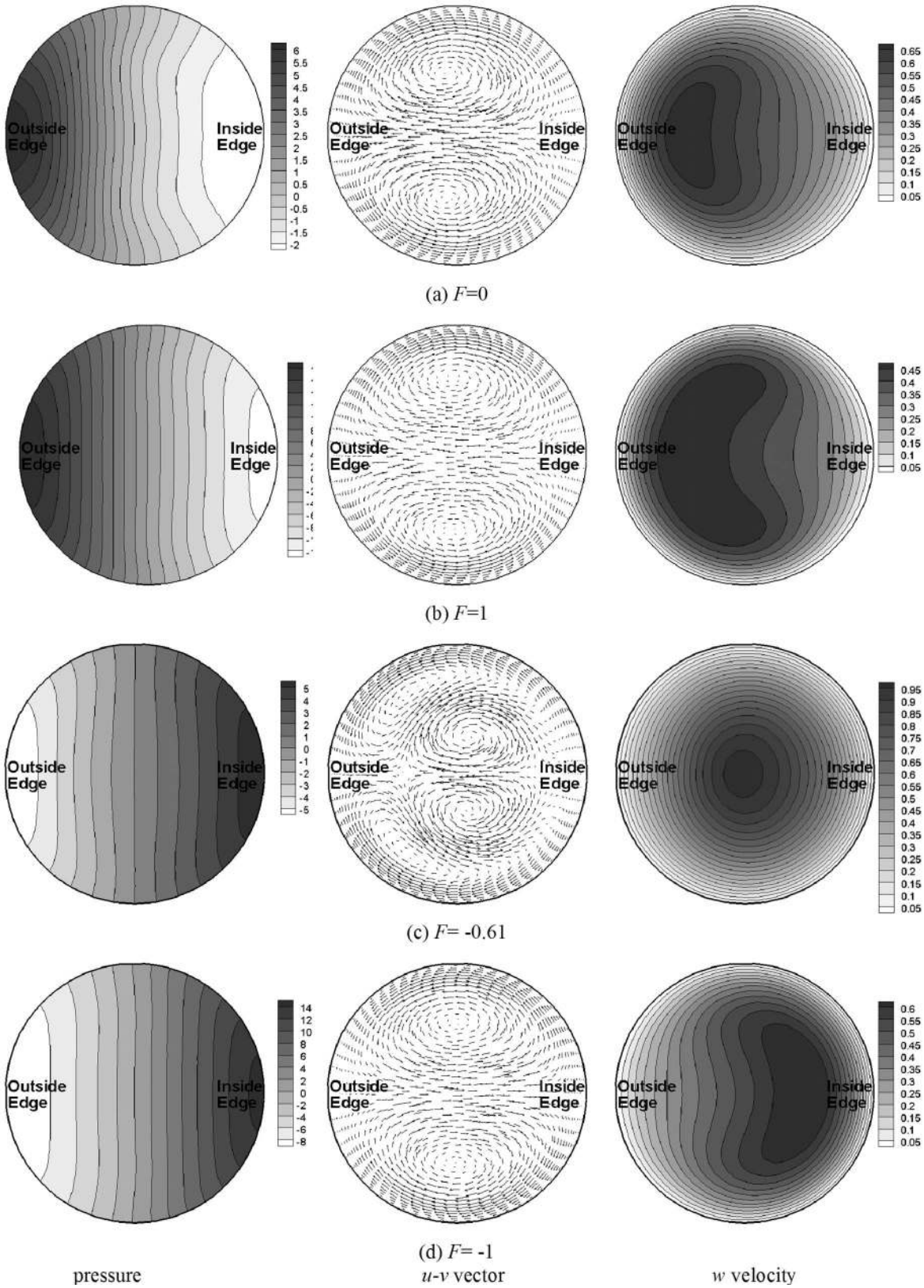

FIG. 3. Pressure, u-v vector, and w velocity on the cross section for different F numbers (Dn=63.25, κ=0.1). (a) F=0. (b) F=1. (c) F=−0.61. (d) F=−1.

outside edge flows toward inside edge, and a secondary boundary layer develops on the wall. A pair of counter-rotating vortices placed symmetrically with respect to the plane of symmetry, upper clockwise, and lower anticlockwise can be observed. Such vortices were also reported by Pui *et al.*[22] When the pipe corotates (F=1) as shown in Fig. 3(b), both the centrifugal force and the Coriolis force on cross section act radially outward and two kinds of second-

ary flows in the same direction are superimposed. The rotation enhances the effect of the curvature on the flow behavior so the secondary flow has the same pattern and the same direction as that for the stationary case with a two vortices structure. The pressure contour line with zero value, therefore, shifts outside edge of the bend, and the margin of the maximum and the minimum pressure increases. As a result of the Coriolis force's effect, the region with high axial velocity tends to be elongated. When the pipe counter-rotates ($F<0$) as shown in Figs. 3(c) and 3(d), the Coriolis force and the centrifugal force are pointed to the opposite directions. When $|F|$ is small, the two forces have the same order of magnitude (also see Ref. 21). They counteract each other and have a contrary effect on the secondary flow on the cross section. At the same time, the new two counter-rotating vortices with opposite directions to primary vortices occur near to the symmetrical line. The axial velocity contours are therefore similar to the case for the straight pipe. As $|F|$ becomes high enough, the Coriolis force will dominate the secondary flow, and the new two opposite vortices will replace the primary two vortices. The region with large axial velocity is pushed toward inside edge of the bend.

B. Distributions of nanoparticle mass fraction

The distributions of nanoparticle mass fraction for different Schmidt numbers and F numbers are shown in Fig. 4. As shown in Eq. (15), the nanoparticle transport in a rotating curved pipe is controlled by the Reynolds number, Schmidt number, nondimensional curvature, and F number, which is dependent on the flow velocity (the Reynolds number and nondimensional curvature can be combined into the Dean number). At the left side of Eq. (15), there are two parts: $\mathrm{Re}\,\mathrm{Sc}[u(\partial Q/\partial r)+(v/r)(\partial Q/\partial\theta)]$ and $\mathrm{Re}(w/M)$. The first part is the contribution of the secondary flow on the cross section to the distributions of nanoparticle mass fraction, and the second part is caused by the axial flow. When Schmidt number is small and the velocity of the secondary flow is several orders of magnitude less than that of the main axial flow, the first part can be ignored. The nanoparticle distributions in these cases are mostly determined by the axial velocity, as shown in Fig. 4(a). The pattern of nanoparticle distribution is a series of concentric closed lines. When the Schmidt number is many orders of magnitude larger than 1, the secondary flow on the cross section will dominate the nanoparticle distribution, which becomes symmetrical with respect to the top and bottom sides of the bend. The nanoparticle distribution is similar to the secondary flow patterns, as shown in Fig. 4(b), and we can find that the concentration gradients at the center of the secondary flow region are much smaller than that at the neighborhood of the edge. It means that the nanoparticles are more uniformly distributed. Shi *et al.*[15] simulated the nanoparticle concentration distribution of $d_p=1$ nm, 150 nm in the double bifurcation region (for only stationary case), and also give similar results.

As discussed above, the rotation with $F=1$ only enhances the effect on the secondary flow caused by the curvature in case of $F=0$ so the nanoparticle distributions for $F=1$ and $F=0$ are similar as a whole. The difference is that the maximum of nanoparticle mass fraction for $F=1$ is a little smaller than that for $F=0$.

When the pipe counter-rotates ($F<0$), the Coriolis force caused by the rotation is in the opposite directions to the centrifugal force. For the case with small Schmidt number, the region with high value of nanoparticle mass fraction is pushed toward inside edge of the bend. So the pattern of nanoparticle distribution for $F=-0.61$ is a series of concentric circles with the maximum located near the center of the bend, while the maximum is located close to the inside edge for $F=-1$. The nanoparticle distributions with large Schmidt number for $F=-0.61$ are different from others because of the complicated pattern of the secondary flow. There are four regions with high value placed at the center of the vortices on the cross section. The maximum of nanoparticle mass fraction first increases, as shown in $F=-0.61$, and then decreases with decreasing F further.

C. Nanoparticle deposition

It is mentioned before that in the simulation of Zhang and Kleinstreuer,[13] nanoparticle deposition for steady flow is similar to those for cyclic inspiratory flow in which the deposition analyses of nanoparticles has gained considerable attention because of the increasing awareness of toxic particle effects and, in turn, the advantages of therapeutic drug aerosol inhalation.[15] Thus the discussion here about the nanoparticle deposition in curved pipe for laminar steady flow is more or less helpful to the lung treatment.

Figure 5 shows the variation of DEF with respect to θ on the edge of bend for different Dean and Schmidt numbers. The relation of Schmidt number and particle diameter is given in Table I. The curves of DEF for the stationary and counter-rotation cases with small Dean number are shown in Figs. 5(a)–5(c). In the stationary case, as shown in Fig. 5(a), the maximum DEF for different Schmidt numbers occurs at the outside edge of the bend with $\theta=\pi$, while the minimum occurs at the inside edge with $\theta=0$. It means that there is a "hot spot" deposition region near outside edge as expected. As the Schmidt number increases, the maximum DEF increases and the minimum DEF decreases. In other words, for the case with larger Schmidt number, the effect of the secondary flow on the cross section is more obvious. The secondary flow will carry the nanoparticles in the center region toward the edge. As a result, the particle deposition will become more possible. However when the Schmidt number is large enough (e.g., $d_p=50$ nm), the variation of DEF is slight because of the low diffusivity and low capacity of mixing. The similar phenomena can also be observed in the counter-rotation cases, as shown in Figs. 5(b) and 5(c), where the Coriolis force makes the nanoparticle distribution almost opposite to the stationary case and hence the hot spots deposition region occurs inside the edge of the bend ($\theta=0$), while the weakest deposition region occurs at the outside edge. Something special for the case of $d_p=0.5$ nm is that

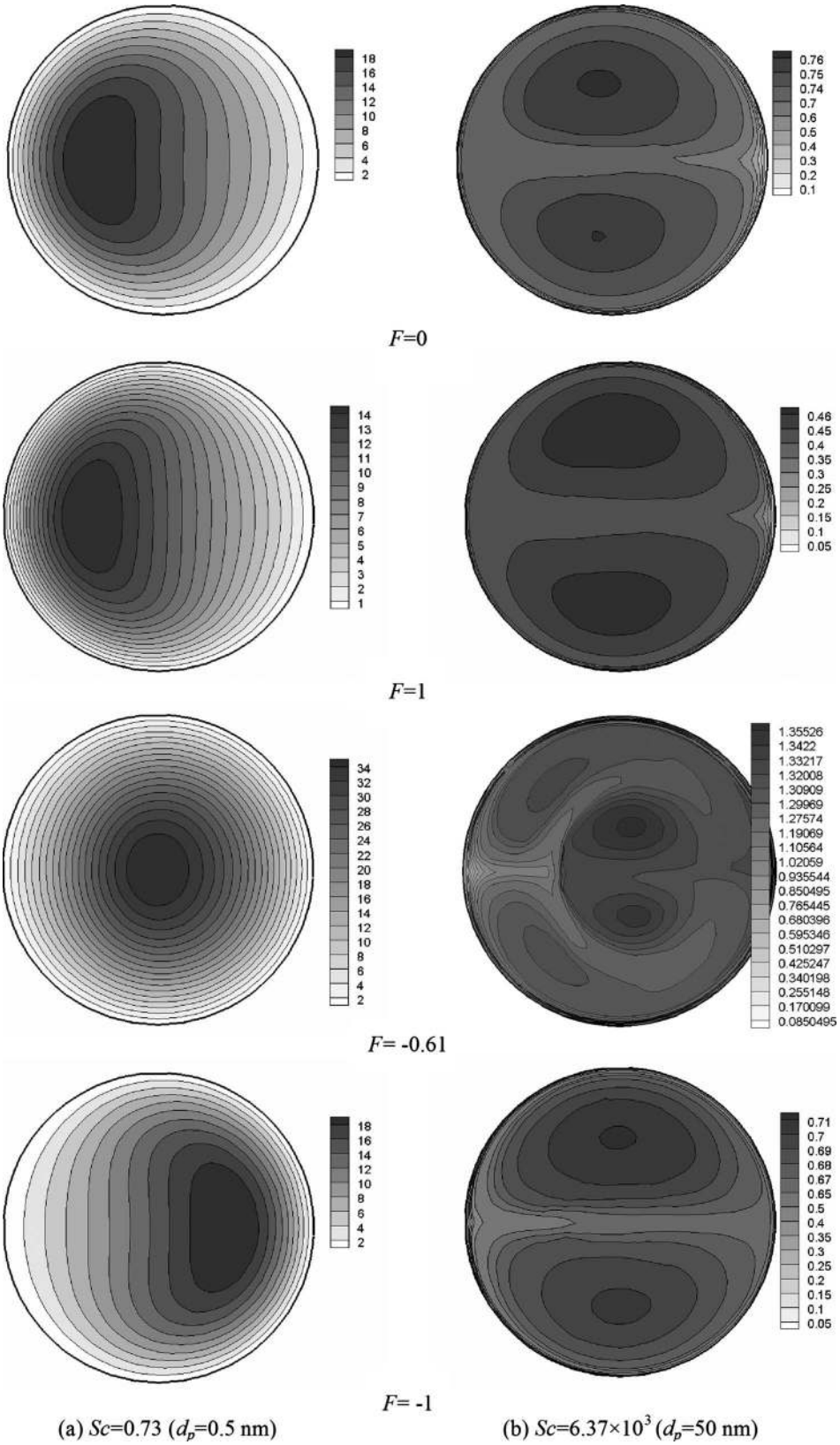

FIG. 4. Nanoparticle distributions for different F numbers and Schmidt numbers. (a) Sc=0.73 (d_p=0.5 nm). (b) Sc=6.37×10^3 (d_p=50 nm).

the DEF all over the edge is close to the line of DEF=1 (which is the mean value of the DEF on the whole wall). It demonstrated that the nanoparticles with small Schmidt number deposit on the whole pipe wall homogeneously because of the tiny difference in the nanoparticle concentration gradient near the edge.

Figures 5(d) and 5(e) show the curves of DEF for the stationary and corotation cases with large Dean number. When the pipe corotates, the curves of DEF are mainly similar to that for the stationary case because of the similar flow field between the two cases. Comparing Figs. 5(a) and 5(d), we can find that with increasing Dean number, the curves of

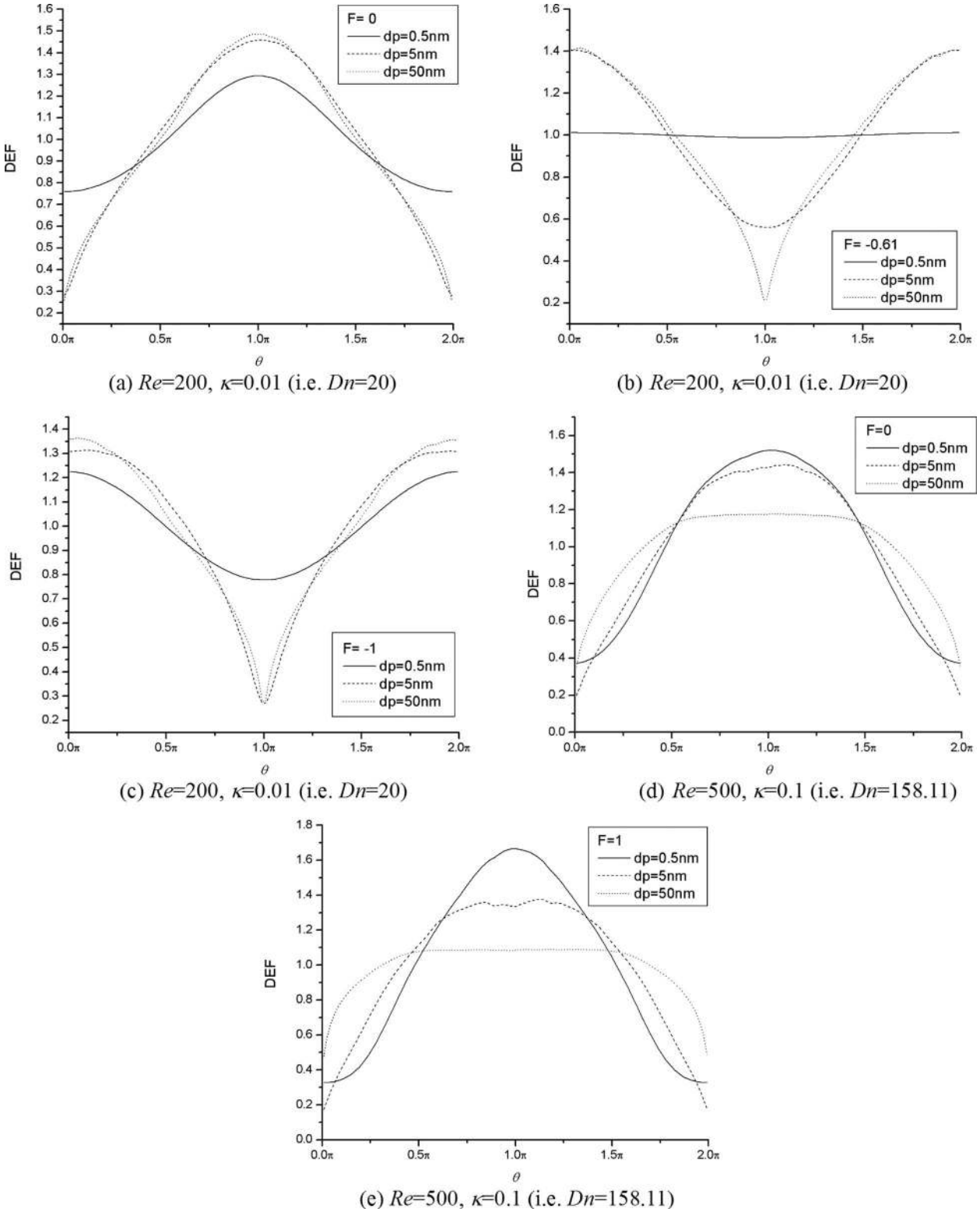

FIG. 5. The DEF for different nanoparticle diameters and F numbers. (a) Re=200, κ=0.01 (i.e., Dn=20). (b) Re=200 and κ=0.01 (i.e., Dn=20). (c) Re =200 and κ=0.01 (i.e., Dn=20). (d) Re=500 and κ=0.1 (i.e., Dn=158.11). (e) Re=500 and κ=0.1 (i.e., Dn=158.11).

DEF become smoother because a higher Dean number offers a lower chance for the nanoparticles to deposit in a shorter residence time, especially for the case with large Schmidt number (e.g., d_p=50 nm). The corotation of pipe also makes the curves of DEF smoother. It indicates that the particle deposition over the whole edge of the bend is more uniform.

D. Relative deposition efficiency

The variations of relative deposition efficiency η_r with Schmidt number for different Dean numbers are shown in Fig. 6. We can see that the corotation (F=1) makes the deposition efficiency a reduction because the curves of η_r for F

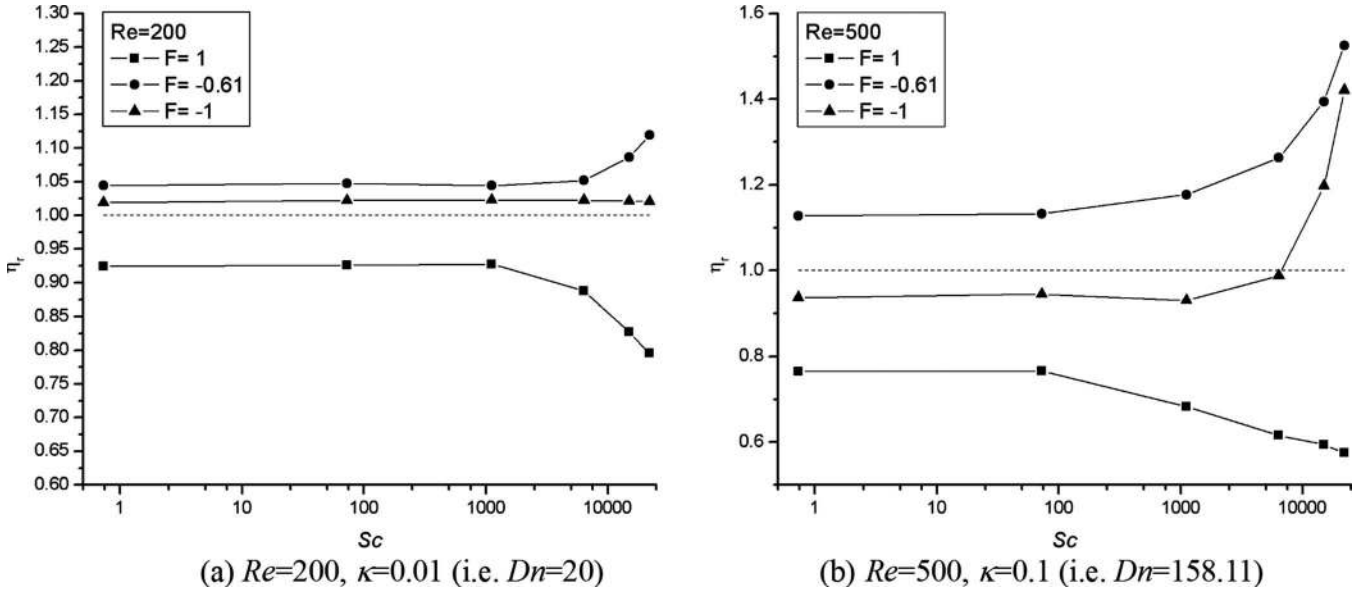

FIG. 6. η_r with respect to Schmidt number for different Dean numbers. (a) Re=200 and κ=0.01 (i.e., Dn=20). (b) Re=500 and κ=0.1 (i.e., Dn=158.11).

=1 are less than 1. The amount of reduction is large for the cases with higher Schmidt and Dean numbers. As mentioned above, the secondary flow caused by the Coriolis force acts in the same direction as that caused by the curvature when the pipe is corotating so the effect of the corotation on the flow is similar to that of the Dean number. For the case with larger Dean number, the residence time of nanoparticle deposition is shorter. Therefore, the deposition efficiency is decreased comparing to the stationary case. When two kinds of secondary flows on the cross section are coexisting, i.e., $F=-0.61$, the values of η_r are larger than 1 because more nanoparticles are carried to the edge thus, have a higher opportunity to deposit. When the secondary flow caused by the Coriolis force dominates the flow, i.e., $F=-1$, the values of η_r are close to 1 until the Schmidt number becomes very large. It demonstrates that the high counter-rotation only slightly affects the particle deposition efficiency. When the Schmidt number is large enough, the effect of rotation on the values of η_r is very obvious.

V. CONCLUSIONS

The transport and deposition of nanoparticles in a rotating curved pipe with circular cross section are simulated numerically for different angular velocities, Dean numbers, and Schmidt numbers. A finite-volume code and the SIMPLE scheme are used to solve the equations. The following conclusions are drawn.

When the pipe corotates ($F>0$), two kinds of secondary flows in the same direction caused by the Coriolis force and the centrifugal force are superimposed. For the case that the pipe counter-rotates ($F<0$), the new two counter-rotating vortices with opposite directions to primary occur when $|F|$ is small. When $|F|$ is high enough, the new two vortices with opposite directions will take place of the two primary vortices.

When the Schmidt number is small, the nanoparticle distributions are mostly determined by the axial velocity. When the Schmidt number is many orders of magnitude larger than 1, the secondary flow will dominate the nanoparticle distribution.

When the pipe corotates ($F>0$), the distributions of nanoparticle mass fraction are similar to that for the stationary case ($F=0$). When the pipe counter-rotates ($F<0$), the Coriolis force pushes the region with high value of nanoparticle mass fraction toward inside edge of the bend.

When the pipe corotates or keeps stationary ($F\geq 0$), there is a hot spot deposition region near the outside edge. When the pipe counter-rotates ($F<0$), the hot spot point appears at the inside edge. The particle deposition over the whole edge of the bend becomes uniform as the Dean number increases.

The corotation of the pipe makes the particle deposition efficiency a reduction, while high counter-rotation of the pipe only slightly affects the deposition efficiency. When two kinds of secondary flows are coexisting, the relative deposition efficiency is larger than that for the stationary case.

ACKNOWLEDGMENTS

This work was supported by the Key Project of the National Natural Science Foundation of China (Grant No. 10632070).

[1] S. K. Friedlander, *Smoke, Dust, and Haze: Fundamentals of Aerosol Dynamics*, 2nd ed. (Oxford University Press, Oxford, 2000).
[2] D. B. Kittelson, "Engines and nanoparticles: A review," J. Aerosol Sci. **29**, 575 (1998).
[3] M. Z. Yu, J. Z. Lin, L. H. Chen, and T. L. Chan, "Large eddy simulation of a planar jet flow with nanoparticle coagulation," Acta Mech. Sin. **22**, 293 (2006).
[4] T. L. Chan, J. Z. Lin, K. Zhou, and C. K. Chan, "Simultaneous numerical simulation of nano and fine particle coagulation and dispersion in a round jet," J. Aerosol Sci. **37**, 1545 (2006).
[5] J. Z. Lin, T. L. Chan, S. Liu, K. Zhou, Y. Zhou, and S. C. Lee, "Effects of coherent structures on nanoparticle coagulation and dispersion in a round jet," Int. J. Nonlinear Sci. Numer. Simul. **8**, 45 (2007).
[6] M. Z. Yu, J. Z. Lin, and T. L. Chan, "Numerical simulation of nanoparticle synthesis in diffusion flame reactor," Powder Technol. **181**, 9 (2008).

[7]M. Z. Yu, J. Z. Lin, and T. L. Chan, "Effect of precursor loading on non-spherical TiO2 nanoparticle synthesis in a diffusion flame reactor," Chem. Eng. Sci. **63**, 2317 (2008).
[8]P. Daskopoulos and A. M. Lenhoff, "Flow in curved ducts. Part 2. Rotating ducts," J. Fluid Mech. **217**, 575 (1990).
[9]J. Ma, X. Shen, B. Zhang, and H. J. Chen, "Numerical analysis of the fluid flow in a rotating curved elliptical pipe, " J. Hydrodynam. **17**, 171 (2005).
[10]H. Ishigaki, "Laminar convective heat transfer in rotating curved pipes," JSME Int. J., Ser. B **42**, 489 (1999).
[11]J. Wang, R. C. Flagan, and J. H. Seinfeld, "Diffusional losses in particle sampling systems containing bends and elbows," J. Aerosol Sci. **33**, 843 (2002).
[12]J. Malet, L. Alloul, N. Michielsen, D. Boulaud, and A. Renoux, "Deposition of nanosized particles in cylindrical tubes under laminar and turbulent flow conditions," J. Aerosol Sci. **31**, 335 (2000).
[13]Z. Zhang and C. Kleinstreuer, "Airflow structures and nano-particle deposition in a human upper airway model," J. Comput. Phys. **198**, 178 (2004).
[14]P. F. Lin and J. Z. Lin, "Transport and deposition of nanoparticles in bend tube with circular cross-section," Prog. Nat. Sci. **19**, 33 (2009).
[15]H. Shi, C. Kleinstreuer, Z. Zhang, and C. S. Kim, "Nanoparticle transport and deposition in bifurcating tubes with different inlet conditions," Phys. Fluids **16**, 2199 (2004).
[16]A. M. Robertson and S. J. Muller, "Flow of Oldroyd-B fluids in curved pipes of circular and annular cross-section," Int. J. Non-linear Mech. **31**, 1 (1996).
[17]D. E. Olson and B. Snyder, "The upstream scale of flow development in curved circular pipes," J. Fluid Mech. **150**, 139 (1985).
[18]H. Ishigaki, "Analogy between developing laminar flows in curved pipes and orthogonally rotating pipes," JSME Int. J., Ser. B **42**, 197 (1999).
[19]J. Ma, X. Shen, M. Zhang, and B. Zhang, "Laminar developing flow in the entrance region of rotating curved pipes," J. Hydrodynam. **18**, 418 (2006).
[20]S. V. Patankar, *Numerical Heat Transfer and Fluid Flow* (Hemisphere, New York, 1980).
[21]H. Ishigaki, "Laminar flow in rotating curved pipes," J. Fluid Mech. **329**, 373 (1996).
[22]D. Y. H. Pui, F. Romay-Novas, and B. Y. H. Liu, "Experimental study of particle deposition in bends of circular cross section," Aerosol Sci. Technol. **7**, 301 (1987).
[23]H. Chen, B. Zhang, and J. Ma, "Theoretical and numerical analysis of convective heat transfer in the rotating helical pipes," Int. J. Heat Mass Transfer **46**, 4899 (2003).